

# Blink: Dynamic Visual Token Resolution for Enhanced Multimodal Understanding

Yuchen Feng<sup>1,2\*</sup>, Zhenyu Zhang<sup>3\*</sup>, Naibin Gu<sup>1,2</sup>, Yilong Chen<sup>1,2</sup>, Peng Fu<sup>1,2‡</sup>, Zheng Lin<sup>1,2</sup>, Shuohuan Wang<sup>3</sup>, Yu Sun<sup>3</sup>, Hua Wu<sup>3</sup>, Weiping Wang<sup>1</sup>, Haifeng Wang<sup>3</sup>,

<sup>1</sup>Institute of Information Engineering, Chinese Academy of Sciences, Beijing, China

<sup>2</sup>School of Cyber Security, University of Chinese Academy of Sciences, Beijing, China

<sup>3</sup>Baidu Inc., Beijing, China

{fengyuchen, fupeng}@iie.ac.cn, zhangzhenyu07@baidu.com

## Abstract

Multimodal large language models (MLLMs) have achieved remarkable progress on various vision-language tasks, yet their visual perception remains limited. Humans, in comparison, perceive complex scenes efficiently by dynamically scanning and focusing on salient regions in a sequential “blink-like” process. Motivated by this strategy, we first investigate whether MLLMs exhibit similar behavior. Our pilot analysis reveals that MLLMs naturally attend to different visual regions across layers and that selectively allocating more computation to salient tokens can enhance visual perception. Building on this insight, we propose Blink, a dynamic visual token resolution framework that emulates the human-inspired process within a single forward pass. Specifically, Blink includes two modules: saliency-guided scanning and dynamic token resolution. It first estimates the saliency of visual tokens in each layer based on the attention map, and extends important tokens through a plug-and-play token super-resolution (TokenSR) module. In the next layer, it drops the extended tokens when they lose focus. This dynamic mechanism balances broad exploration and fine-grained focus, thereby enhancing visual perception adaptively and efficiently. Extensive experiments validate Blink, demonstrating its effectiveness in enhancing visual perception and multimodal understanding.

## 1. Introduction

Multimodal large language models (MLLMs) have rapidly emerged across various downstream fields, including computer vision and natural language processing [1, 4, 10, 26, 41]. By coupling a vision encoder with a projector that

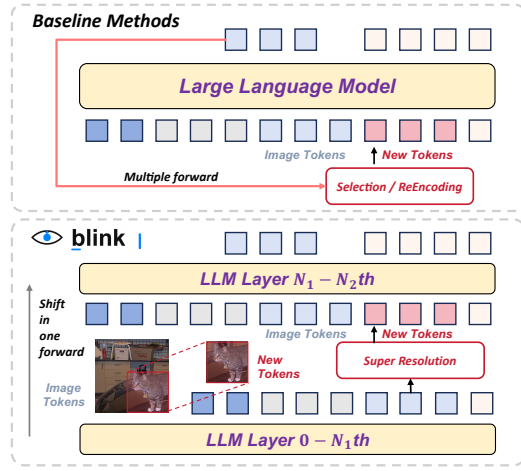


Figure 1. Comparison of the conventional post-hoc paradigm for enhancing salient regions, and our propose Blink. Blink shifts attention across salient regions over layers, achieving dynamic visual perception enhancement.

maps visual features into the language space of the following LLM, MLLMs effectively unify visual and textual representations [2, 28, 32]. This architecture has demonstrated impressive performance across a wide spectrum of multimodal tasks, including text generation, visual understanding, and cross-modal reasoning. Despite these advances, MLLMs still struggle with insufficient visual perception capabilities [11, 45], often resulting in incorrect answers or hallucinated explanations [5, 15, 22, 42]. Compared with LLMs, MLLMs take additional visual inputs and thus need to reason over both linguistic and visual information, making their performance on multimodal tasks highly dependent on visual perception. However, current MLLMs still adopt the conventional LLM architecture for downstream task execution, lack of explicitly enhancing or leveraging

\* Equal Contribution.

† Work done during internship at Baidu Inc.

‡ Corresponding Author.

salient visual regions [6, 46, 52]. Therefore, it is imperative to investigate their visual perception to reveal potential risks in downstream applications.

Unlike naive textual understanding, humans perceive visual scenes through a progressive and dynamic process. They first glance the entire image, then fixate on salient regions, and subsequently shift attention to new areas when the current focus becomes uninformative, as studied in cognitive and visual neuroscience [12, 18, 23, 36]. This dynamic process, reminiscent of a rapid “blink” between salient regions, enables humans to efficiently integrate visual information through sequential attention shifts. Inspired by this principle, it is quite promising to equip MLLMs with a similar capability that detects and selects salient regions, adaptively expands attention on them, and shifts focus as needed, thereby progressively guiding the model toward the most informative areas.

To explore a possible solution, we conduct a pilot analysis of MLLMs’ visual information processing behavior and uncover **two key insights**, across and within transformer layers. Across layers, the attention weights vary substantially, suggesting that different layers focus on distinct visual regions with varying attention sharpness. Within a layer, we find that increasing computation for high-attention visual tokens, such as replicating salient regions, effectively enhance the visual perception capability. *These findings reveal that MLLMs possess an inherent ability to attend to diverse regions across layers and improve visual understanding by allocating more computation to salient tokens.* Recent approaches have attempted to identify salient regions by utilizing attention maps or post-hoc selection modules, and improve visual perception through two or more forward pass [9, 27, 45, 49, 51]. However, since an image often contain multiple salient regions, these post-hoc methods typically only support focusing on one salient region, thereby limiting both flexibility and efficiency. It raises a natural question: *How can we dynamically enhance the visual perception capability of MLLMs within one forward pass?*

Building upon these observations, we propose **Blink**, a dynamic visual token resolution framework that emulates human-like scanning and focusing within a single forward pass of MLLMs. Inspired by the human strategy of alternating between broad visual exploration and fine-grained attention, Blink is designed to dynamically allocate more tokens to salient visual regions, enhancing multimodal understanding without multiple inference steps. Specifically, it consists of two synergistic modules: saliency-guided scanning and dynamic token resolution. In the inference process, it first scans the attention map to estimate the saliency of visual tokens, and then expands the selected salient regions through a trained amplifier token super-resolution module. As attention shifts away, the corresponding visual tokens are pruned, allowing a dynamic balance between wide-area

scanning and detail focusing. As shown in Fig. 1, by mimicking this human-like perception strategy, Blink leverages the inherent non-uniformity of attention across transformer layers, enabling adaptive enhancement of visual perception and improving overall model performance.

We conduct experiments on LLaVA-1.5 [32] across seven vision-language benchmarks. Our method achieves consistent performance improvement compared with the backbone model, demonstrating notable gains in visual perception and understanding. Even in the variant where the token super-resolution module is replaced with simple training-free interpolation and only the inference pipeline is retained, Blink still surpasses the backbone, confirming the effectiveness of our dynamic framework. Furthermore, comprehensive analyses highlight the contributions of key modules and design choices, while providing insights into the underlying mechanisms of our approach.

In summary, our contributions are threefold:

- **Key Insights.** We reveal two previously overlooked properties of MLLMs, showing that the visual focus naturally shifts across layers and selectively allocating computation to salient regions yields stronger visual perception.
- **Dynamic Framework.** We propose Blink, a dynamic visual token resolution framework that enables adaptive enhancement of multimodal understanding by expanding salient tokens and dropping less informative regions.
- **Empirical Evaluation.** We validate Blink across diverse multimodal benchmarks, demonstrating consistent improvements in visual perception and establishing a simple yet effective plug-in mechanism for enhancing MLLMs.

## 2. Preliminary

### 2.1. Architecture of MLLMs

An MLLM typically consists of a vision encoder  $F_v(\cdot)$ , a projection network  $F_p(\cdot)$ , and a stack of transformer-based decoder layers that serve as the LLM backbone. Given an input image  $I \in \mathbb{R}^{H \times W \times 3}$ , a textual prompt  $T$ , and a system prompt  $S$ , the vision encoder first extracts visual features  $E_v = F_v(I) \in \mathbb{R}^{h \times w \times d}$ , which are projected into the LLM embedding space as  $\tilde{E}_v = F_p(E_v) \in \mathbb{R}^{h \times w \times d}$ . Meanwhile, the textual prompt with  $n$  tokens is embedded as  $E_t \in \mathbb{R}^{n \times d}$ . Next, the hidden states are combined as  $hs^{(0)} = \text{concat}(\tilde{E}_v, E_t)$ , and fed into  $L$  decoder layers. Each layer includes a multi-head self-attention (MHA) module and a feed-forward network (FFN) with residual connections. Finally, after all decoder layers, the last hidden states  $hs^{(L)}$  are mapped to the vocabulary space via an output projection matrix  $W_O \in \mathbb{R}^{d \times V}$ , and normalized by Softmax to produce the next-token probabilities. In this way, LLM generates tokens in the form of auto-regression based on both visual and textual inputs, integrating multimodal information at each step.

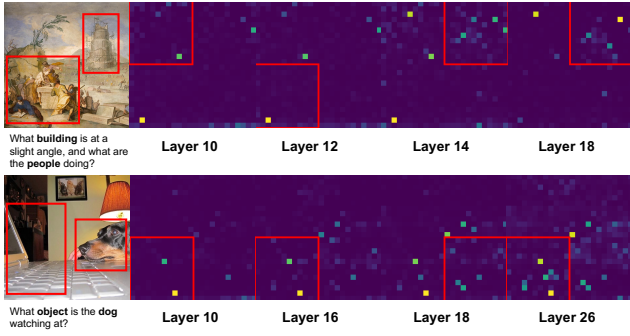


Figure 2. Visualization of attention maps across layers. In the right panels, lighter colors indicate higher attention from the last text token, and red boxes highlight the region with the highest total attention weights.

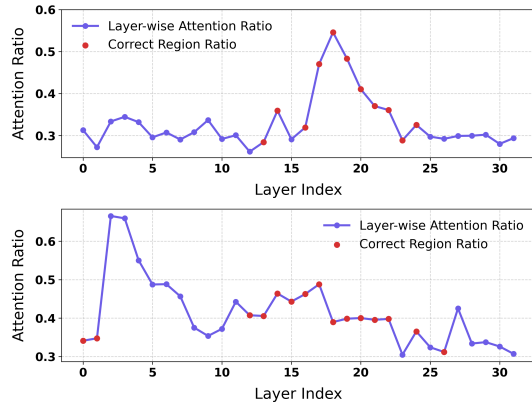


Figure 3. Attention ratio across layers. Purple lines indicate the ratio of attention weights in the most attended region to the total attention over all visual tokens, and red dots mark layers where the most attended region is correct.

## 2.2. Key Insights

To better understand how MLLMs leverage multimodal information, we take a deep dive into model behaviors both across and within transformer layers. These studies reveal two key insights into how MLLMs perceive and utilize visual information.

**Key Insight 1: Attention weights are non-uniformly distributed across layers.** Here, we explore how MLLMs distribute attention over image regions relevant to the text input as the signals propagate across layers. Inspired by prior studies that leverage attention maps to assess token importance [7, 8, 43, 47, 48], we analyze how attention distributions vary across layers in LLaVA-1.5-7B.

We first examine how attention patterns evolve across layers when processing an image. In Fig. 2, we treat the final text token as the query and compute attention weights over all visual tokens. For visualization, the attention maps in each layer are reshaped to  $H \times W$  to match the spatial

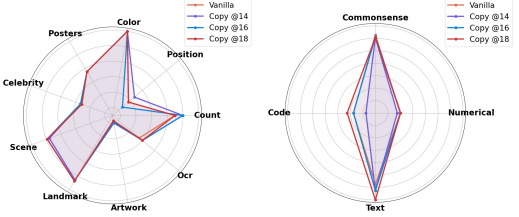


Figure 4. Performance on MME tasks when copying salient visual tokens at different layers. Vanilla denotes the original LLaVA-1.5 performance, and Copy @14/16/18 indicates the layer at which token copying is applied.

layout of the original image, and we highlight the region with the highest cumulative attention weight. It is observed that when multiple important targets exist in an image (e.g., the building and people in Case 1, or the object and dog in Case 2), the attention does not remain fixed on a single region. Instead, it progressively shifts its focus over different regions across layers. This behavior indicates that the model inherently possesses the ability to refine its attention progressively and to switch focus among multiple objects.

Furthermore, we analyze how the attention ratio evolves across layers, where the ratio is defined as the attention weight of the most attended region relative to the total visual attention. As shown in Fig. 3, the purple curve tracks this ratio across transformer depth, and red markers indicate layers where the attended region corresponds to the correct visual area. Two patterns emerge: (1) correct attention tends to occur in the middle layers (approximately layers 12–26), and (2) these layers show notably sharper attention distributions, reflecting greater model confidence when focusing on relevant regions. Taken together, the above analyses reveal our first insight that different transformer layers exhibit distinct attention patterns, which progressively shift focus across layers and differ in sharpness.

**Key Insight 2: The computation on salient visual tokens within a layer affects visual perception.** Next, to investigate the effect of computation on salient visual regions within a layer, we copy the visual tokens corresponding to the highest-attention areas at a given layer. These copied tokens are interpolated to match the original sequence length and inserted between the original visual tokens and the text token embeddings in the hidden states. Subsequent layers then process this extended sequence, effectively increasing the computational focus on important regions.

Fig. 4 shows the evaluation on several perception and cognition tasks in a representative benchmark, MME [17]. Specifically, it compares the performance of the vanilla LLaVA-1.5 model with that of models where token copying is applied at fixed layers (14, 16, and 18). In the radar plots, a larger enclosed area indicates better task performance, clearly showing that when we copy salient visual

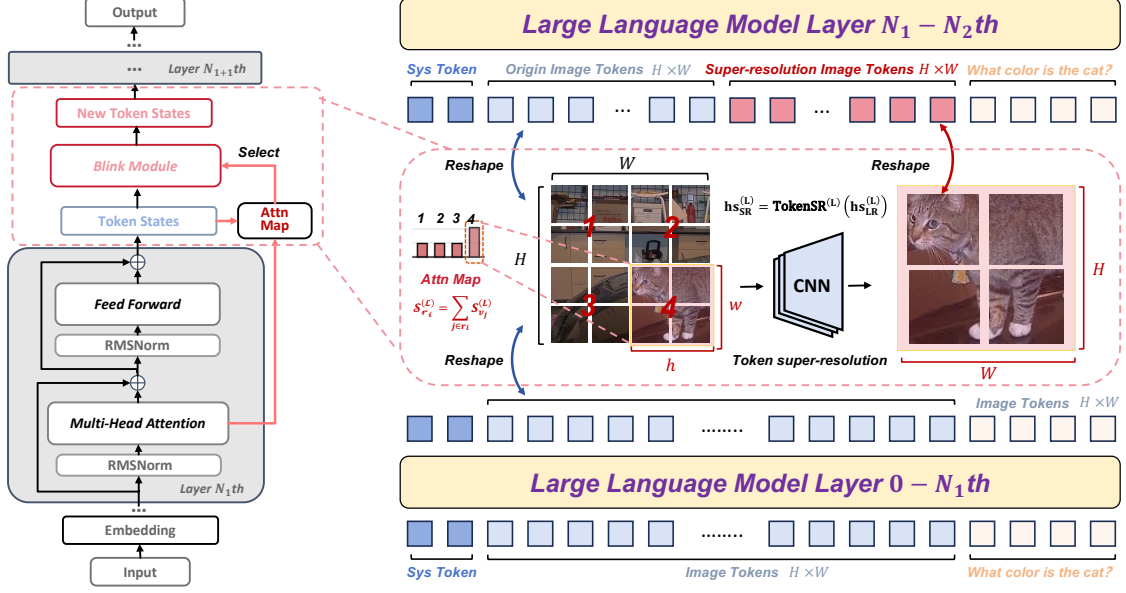


Figure 5. Illustration of our proposed Blink. The left side shows the saliency-guided scanning that determines whether to expand or drop visual tokens across transformer layers. The right side shows within-layer sequence reconstruction, where salient tokens are amplified by the token super-resolution module.

tokens at fixed layers, thereby increasing computation on important regions, the performance improves across tasks. These findings form our second insight that allocating more computation to salient visual tokens within a layer can enhance the visual perception capability of MLLMs.

These two insights reveal that MLLMs inherently adjust their visual focus both across and within layers and that dynamically allocating computation to salient regions can further enhance their perception capability. *They motivate us to design a framework exploiting these properties to achieve adaptive visual perception enhancement.*

### 3. Method

In this section, we propose the Blink framework. As shown in Fig. 5, Blink comprises two modules: saliency-guided scanning and dynamic token resolution, simulating human-like rapid scanning and focusing, thereby it can enhance visual perception within a single forward pass in an efficient and adaptive manner.

#### 3.1. Saliency-Guided Scanning

As discussed in Sec. 2.2, salient visual tokens can be intuitively identified as those receiving higher attention scores. Based on it, we calculate the saliency of each visual token with respect to the last token of the text prompt using. At each involved transformer layer  $L$ , we denote the hidden states of the visual tokens and the final text token as  $h_{s_v}^{(L)}$  and  $h_{s_{t_n}}^{(L)}$ , respectively. The corresponding key and query

representations are obtained through linear projections:

$$k_v^{(L)} = K_v(h_{s_v}^{(L)}), \quad q_{t_n}^{(L)} = Q_t(h_{s_{t_n}}^{(L)}), \quad (1)$$

where  $K_v(\cdot)$  and  $Q_t(\cdot)$  represent the key and query projection matrices of the MHA module. The saliency score  $S_v^{(L)}$  of each visual token is then computed as the similarity between  $q_{t_n}^{(L)}$  and  $k_v^{(L)}$ :

$$S_v^{(L)} = q_{t_n}^{(L)}(k_v^{(L)})^\top. \quad (2)$$

To recover the original spatial structure of the image, we reshape the one-dimensional sequence of visual tokens into a two-dimensional grid of size  $H \times W$ , corresponding to the spatial layout of the input image. The grid is uniformly divided into  $p \times p$  non-overlapping patches of equal size, each with dimensions  $h \times w = \left(\frac{H}{p}\right) \times \left(\frac{W}{p}\right)$ . For each patch  $r_i$ , we compute its aggregated saliency as the sum of token-level scores  $S_{r_i}^{(L)} = \sum_{j \in r_i} S_{v_j}^{(L)}$ . The patch with the highest aggregated saliency is identified as the most informative region at layer  $L$ .

Building on our insight that different layers exhibit distinct attention distributions, including variations in both the most attended regions and the sharpness of these attention peaks, we observe that the model progressively attends to multiple potential regions of interest across layers, with varying degrees of saliency concentration. Following this observation, we further define a saliency ratio between the

most salient patch and all visual tokens:

$$\rho^{(L)} = \frac{\mathcal{S}_{r_{\max}}^{(L)}}{\sum_i \mathcal{S}_{r_i}^{(L)}}, \quad (3)$$

where  $\mathcal{S}_{r_{\max}}^{(L)}$  denotes the saliency of the most informative patch at layer  $L$ . The saliency ratio  $\rho^{(L)}$  quantifies the sharpness of the saliency distribution, reflecting how concentrated the attention is at a specific layer. Higher values of  $\rho^{(L)}$  indicate a sharp and localized focus, whereas lower values correspond to a more diffuse and exploratory attention pattern. This ratio is further utilized in the following dynamic token resolution module, enabling the model to adaptively refine its visual focus by expanding salient regions for detailed perception and dropping less informative areas, thereby enhancing visual grounding without additional forward passes.

### 3.2. Dynamic Token Resolution

We define token resolution as the spatial granularity encoded in hidden states, indicating how finely each token represents the underlying visual content. Based on the saliency ratio  $\rho^{(L)}$ , we adopt an adaptive thresholding strategy to dynamically determine whether the model should expand or drop visual tokens at each layer, thereby achieving adjustment of token resolution. Specifically, when  $\rho^{(L)} > \tau_{\text{exp}}$ , the model activates the token super-resolution module to enhance and expand tokens within salient regions, where  $\tau_{\text{exp}}$  is a predefined threshold. On the contrary, when  $\rho^{(L)} < \tau_{\text{drop}}$ , redundant tokens are discarded to reduce computational overhead. Next, we provide a detailed description of how the expansion and dropping operations are respectively applied to the corresponding visual tokens.

#### 3.2.1. Token Expansion

**Token super-resolution module.** Inspired by image super-resolution techniques [13, 14, 24], we introduce a trainable token amplifier, termed the token super-resolution (TokenSR) module, to refine visual token representations. At each decoder layer  $L$ , for low-resolution visual tokens  $hs_{LR}^{(L)}$  selected for expansion, the module reconstructs a higher-resolution token sequence  $hs_{SR}^{(L)}$  that captures finer local semantics and structural details:

$$hs_{SR}^{(L)} = \text{TokenSR}^{(L)}(hs_{LR}^{(L)}). \quad (4)$$

Each TokenSR module consists of three convolutional layers with ReLU activations, where each  $\text{Conv}_k$  denotes a 2D convolutional layer with  $c_k$  filters of kernel size  $f_k \times f_k$ . This hierarchical structure allows the module to refine local details, while keeping the overall semantic information consistent across layers. During training, each TokenSR module receives the hidden states of salient regions from a full image  $I_{\text{full}}$  and produces low-resolution tokens  $hs_{SR}^{(L)}$ .

The corresponding cropped image  $I_{\text{crop}}$  provides reference hidden states  $hs_{\text{crop}}^{(L)}$ . The module is trained by minimizing the KL divergence between enhanced and reference tokens. This supervision encourages the TokenSR module to reconstruct high-resolution token representations for salient regions that match the fine-grained structures of the cropped images. Only the parameters of the TokenSR module are updated, while the MLLM backbone remains frozen.

**Sequence reconstruction.** Within the token expansion process, the enhanced tokens produced by the TokenSR module at decoder layer  $L$  are directly inserted between the original visual tokens and the text tokens. For each sample  $i$ , salient patch tokens  $hs_{\text{patch}}^{(L,i)} \in \mathbb{R}^{h \times w \times d}$  are first extracted from the full-image hidden states, reshaped into a 2D feature map, interpolated to  $H \times W$  via bilinear interpolation and processed by the TokenSR module to obtain enhanced tokens  $hs_{\text{SR}}^{(L,i)} \in \mathbb{R}^{H \times W \times d}$ . These enhanced tokens are then flattened into a 1D sequence. The final output sequence of the corresponding decoder layer is constructed as:

$$hs_i^{(L,\text{output})} = [hs_s^{(L,i)}; hs_v^{(L,i)}; hs_{\text{SR}}^{(L,i)}; hs_t^{(L,i)}]. \quad (5)$$

The attention mask and positional embeddings are updated to accommodate the expanded token sequence, ensuring that the transformer correctly attends to the enhanced visual regions while maintaining causal consistency.

#### 3.2.2. Token Drop

Complementary to token expansion, the token drop mechanism prunes low-saliency visual tokens. If saliency ratio  $\rho^{(L)}$  falls below  $\tau_{\text{drop}}$ , the corresponding  $hs_{\text{SR}}^{(L)}$  is removed. And, the sequence is reverted to its original form of:

$$hs_i^{(L,\text{output})} = [hs_s^{(L,i)}; hs_v^{(L,i)}; hs_t^{(L,i)}]. \quad (6)$$

This operation effectively suppresses over-attended yet uninformative areas, preventing weakly supported salient regions from biasing inference and helping subsequent layers focus on more reliable visual evidence.

### 3.3. Workflow of Blink

Overall, the procedure of Blink is summarized in Alg. 1. Blink integrates its two main stages into a unified workflow that adaptively adjusts the visual token resolution within selected decoder layers. By first identifying the most informative visual patches and then selectively expanding or dropping tokens based on saliency, the framework mimics human-like visual attention patterns. All operations are performed before the layer normalization of each corresponding transformer layer, ensuring that the transformer can process dynamically expanded or pruned tokens without modifying the backbone computations.

Method	MME <sub>Perception</sub>										
	Exist.	Count	Pos.	Color	Poster	Celeb.	Scene	Landm.	Artw.	OCR	Total
Vanilla	190.00	155.00	128.33	170.00	<b>147.62</b>	<b>136.76</b>	<b>158.00</b>	<b>163.00</b>	119.50	<b>137.50</b>	1505.72
<i>Blink-interp (Ours)</i>	<b>190.00</b>	<b>160.00</b>	133.33	<b>170.00</b>	<b>147.62</b>	135.88	157.25	<b>163.00</b>	119.50	<b>137.50</b>	1514.08
<i>Blink (Ours)</i>	<b>190.00</b>	<b>160.00</b>	<b>138.33</b>	<b>170.00</b>	147.28	135.88	<b>158.00</b>	<b>163.00</b>	<b>119.75</b>	<b>137.50</b>	<b>1519.74</b>

Method	MME <sub>Cognition</sub>					GQA	MMBench	MMBench <sub>CN</sub>	POPE	SQA <sub>Img</sub>	MM-Vet
	CS	Num	Text	Code	Total						
Vanilla	112.86	70.00	<b>107.50</b>	<b>67.50</b>	357.86	61.93	64.60	58.08	85.17	69.46	32.20
<i>Blink-interp (Ours)</i>	110.71	70.00	<b>107.50</b>	65.00	353.21	61.93	<b>64.69</b>	58.51	85.17	69.51	31.70
<i>Blink (Ours)</i>	<b>114.29</b>	<b>75.00</b>	<b>107.50</b>	65.00	<b>361.79</b>	<b>61.98</b>	<b>64.69</b>	<b>58.59</b>	<b>85.23</b>	<b>69.66</b>	<b>33.40</b>

Table 1. Downstream task performance across multiple benchmarks on LLaVA-1.5. Results of an additional MLLM backbone are provided in Appendix C. Vanilla denotes the base model, and our methods correspond to two configurations of Blink, where -interp indicates the variant that replaces the amplifier with training-free interpolation while retaining the Blink inference pipeline. The best scores are in **bold**.

### Algorithm 1: Workflow of Blink

```

Input: MLLM  $\mathcal{M}$ , selected layers  $\mathcal{L}_{sel}$ , thresholds
 $\tau_{exp}, \tau_{drop}$ , number of divided patches  $p \times p$ 
Output: Updated hidden states  $\{hs^{(L, output)}\}$ 
1 for  $L \in \mathcal{L}_{sel}$  do
2    $\triangleright$  Saliency-Guided Scanning:
3   Reshape  $hs_v^{(L)}$  into  $H \times W$  grid and divide into  $p$ 
   patches;
4   Compute patch saliency  $S_{r_i}^{(L)}$  and saliency ratio  $\rho^{(L)}$ ;
5    $\triangleright$  Dynamic Token Resolution:
6   if  $\rho^{(L)} > \tau_{exp}$  then
7      $\triangleright$  EXPAND:  $hs_{SR}^{(L)} \leftarrow \text{TOKENSR}(hs_{patch}^{(L)})$ ;
8      $hs^{(L, output)} \leftarrow [hs_s^{(L)}; hs_v^{(L)}; hs_{SR}^{(L)}; hs_t^{(L)}]$ ;
9   else
10    if  $\rho^{(L)} < \tau_{drop}$  then
11       $\triangleright$  DROP: remove  $hs_{SR}^{(L)}$ , revert to original
        sequence;
12       $hs^{(L, output)} \leftarrow [hs_s^{(L)}; hs_v^{(L)}; hs_t^{(L)}]$ ;
13    else
14       $\triangleright$  keep  $hs^{(L)}$  unchanged;
15    $\triangleright$  update Attn_mask and Position_ids;
16 return  $\{hs^{(L, output)}\}$ 

```

## 4. Experiments

### 4.1. Experimental Settings

We evaluate our proposed Blink on LLaVA-1.5-7B [32] across seven commonly used multimodal datasets, including MME [17], GQA [20], MMBench, MMBench-CN [34], POPE [29], ScienceQA [35], and MM-Vet [50]. We evaluate Blink and its variant Blink-interp, where the trainable

modules are replaced with bilinear interpolation, while retaining the Blink inference pipeline. For training the token super-resolution modules, we use the processed LLaVA-1.5 training data, which is a composite dataset consisting of COCO [30], GQA [20], OCR-VQA [37], TextVQA [40], and VisualGenome [25]. For each image, we crop it into four quadrants and record their positions relative to the original image. Detailed training hyper-parameters and inference settings can be found in Appendix A and B.

### 4.2. Main Results

Table 1 presents the downstream performance across seven tasks. Our proposed Blink consistently improves total scores of MME<sub>Perception</sub> and MME<sub>Cognition</sub> over the base model, with gains of 14.02 and 3.93, respectively. Additionally, Blink achieves the highest scores on GQA, MMBench, MMBench-CN, POPE, ScienceQA, and MM-Vet. These results demonstrate the impact of Blink in enhancing multimodal understanding and visual perception.

Blink-interp increases the total score of MME<sub>Perception</sub> by 8.36, and despite underperforming on MME<sub>Cognition</sub> and MM-Vet, it surpasses or matches the base model on all other benchmarks. Moreover, the fully trained Blink outperforms Blink-interp on all benchmarks except for MMBench, where Blink-interp achieves comparable performance. These results highlight both the effectiveness of the dynamic inference pipeline and the robustness of the token super-resolution module.

### 4.3. Ablation Studies

**Key Modules.** To validate the effectiveness of our proposed modules, we perform ablation studies using MME benchmark on the two key components of Blink: saliency-guided scanning (SGS) and dynamic token resolution (DTR). In the

Dataset	Method	Key Modules		Ratio Thresholds		
		w/o SGS	w/o DTR	w/o Drop	High $\tau_{\text{exp}}$ / Low $\tau_{\text{drop}}$	High $\tau_{\text{exp}}$
<i>Blink-interp (Ours)</i>						
MME	Perp.	1514.08	1509.83	1514.73	1514.83	1509.83
	Cong.	353.21	355.36	343.93	351.07	355.71
	Total	1867.29	1865.19 <small>-2.10</small>	1858.66 <small>-8.63</small>	1865.90 <small>-1.39</small>	1865.54 <small>-1.75</small> <small>+0.40</small>
<i>Blink (Ours)</i>						
MME	Perp.	1519.74	1519.74	1478.67	1524.74	1509.83
	Cong.	361.79	359.64	361.79	359.29	357.86
	Total	1881.53	1879.38 <small>-2.15</small>	1840.46 <small>-41.07</small>	1884.03 <small>+2.50</small>	1867.69 <small>-13.84</small> <small>+15.99</small>

Table 2. Performance of Blink and its interpolation variant on the MME benchmark across key modules (SGS, DTR) and ratio threshold settings. Rows labeled w/o SGS and w/o DTR show results with the corresponding module removed. High  $\tau_{\text{exp}}$  / Low  $\tau_{\text{drop}}$  denotes high expansion threshold with low drop threshold, while High  $\tau_{\text{exp}}$  denotes high expansion threshold with normal drop threshold.

w/o SGS variant, token selection for expansion or drop is performed randomly, without guidance of saliency maps. In the w/o DTR variant, token operations follow a fixed expand–drop cycle across layers, without dynamically adjusting based on thresholds. As shown in Table 2, removing either SGS or DTR results in notable performance drops for both Blink and its variant Blink-interp. Specifically, removing SGS results in the total score dropping by 2.10 for Blink-interp and 2.15 for Blink, and removing DTR causes a larger decrease of 8.63 for Blink-interp and 41.07 for Blink, underscoring the critical role of both saliency-guided scanning and dynamic token resolution in effective token selection and capturing salient visual information.

**Ratio Thresholds.** We further investigate the impact of different expansion and drop thresholds on performance. Three alternative settings to our main configuration are considered: (1) the extreme case of disabling token drop (w/o Drop), (2) high expansion threshold and low drop threshold (High  $\tau_{\text{exp}}$  / Low  $\tau_{\text{drop}}$ ), and (3) high expansion threshold only (High  $\tau_{\text{exp}}$ ), with the drop threshold kept at its default value. As shown in Table 2, these settings lead to varying performance compared to our default configuration. Specifically, for Blink-interp, the High  $\tau_{\text{exp}}$  setting yields only a marginal improvement of 0.40 in the total score, whereas the w/o Drop and High  $\tau_{\text{exp}}$  / Low  $\tau_{\text{drop}}$  settings reduce performance by 1.39 and 1.75, respectively. For Blink, disabling token drops increases performance by 2.50, while the High  $\tau_{\text{exp}}$  / Low  $\tau_{\text{drop}}$  and High  $\tau_{\text{exp}}$  settings decrease it by 13.84 and 15.99. These results indicate that completely disabling token deletion leads to divergent outcomes, while excessively high expansion thresholds limit effective token expansion, demonstrating that both token expansion and token drop contribute to our framework.

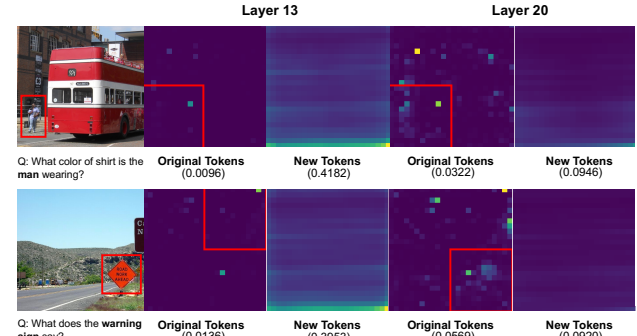


Figure 6. Visualization of attention redistribution after token expansion. Red boxes in the original image indicate the ground-truth important regions. The right panels show attention distributions on the original and expanded visual tokens at layers 13 and 20. See Appendix D for more visualization results.

#### 4.4. Analysis of Attention Redistribution

In this section, we investigate how tokens generated by the token super-resolution module influence attention redistribution across transformer layers after expansion. Understanding this process is important to verify whether the expanded tokens effectively guide the model to focus and contribute to improved visual perception. For clarity, expansion is applied at layer 12, and the new tokens are retained in subsequent layers without dropping.

Fig. 6 shows attention maps at different layers to illustrate this spatial redistribution. In both cases, attention on the new tokens is more evenly distributed than on the original tokens, with their total attention consistently higher, indicating effective focus on the expanded tokens. In Case 2, attention initially targets an incorrect region at layer 13 but shifts to the correct region by layer 20, which is consistent

Layers	Perc.	Cogn.	Total
11–17	1518.20 <sub>-1.54</sub>	364.29 <sub>+2.50</sub>	1882.49 <sub>+0.96</sub>
<i>12–18 (Ours)</i>	1519.74	361.79	1881.53
13–19	1511.97 <sub>-7.77</sub>	362.14 <sub>+0.35</sub>	1874.11 <sub>-7.42</sub>
14–20	1512.06 <sub>-7.68</sub>	362.14 <sub>+0.35</sub>	1874.20 <sub>-7.33</sub>

Table 3. Performance of Blink on the MME benchmark with different ranges of transformer layers. 12–18 denotes the layer range used in our main configuration, and other ranges correspond to alternative settings. The best scores are in **bold**.

with the insight in Sec. 2.2 that the model can progressively adjust attention across layers.

#### 4.5. Analysis of Layer Range

We observe an interesting phenomenon that although selecting intermediate layers (e.g., our 12–18 layer range) generally yields good performance, slight shifts in the chosen layer range can lead to measurable differences in results. As shown in Table 3, we compare several layer selection strategies on the two types of tasks in the MME benchmark as well as the total performance. Shifting from 12–18 to 11–17 slightly improves the total score by 0.96, while shifting to 13–19 or 14–20 results in moderate decreases of 7.42 and 7.33, respectively. These results indicate that different layer ranges contribute differently to the overall performance, and even small changes can lead to non-negligible variations.

To better understand this effect, we further evaluate the importance and contribution of each layer through three analyses: (1) varying the starting layer while fixing the ending layer at 18, (2) fixing the starting layer at 12 while varying the ending layer, and (3) performing dynamic token operations on single layers based on thresholds. As shown in Fig. 7, selecting a single layer leads to clear performance differences, suggesting that attention distributions and accuracy vary across layers. In particular, layers around 7–26 produce much stronger improvements, whereas using only early layers around 4–6 leads to substantial performance drops. Moreover, the choice of layer range affects performance. In the first analysis, excluding layers 4–9 yields better results, whereas in the second analysis, including layers 14–18 causes a noticeable drop. These observations are consistent with Sec. 2.2, where correct attention tends to emerge in the middle layers. And, from the curves marked with our config, it can be seen that we adopt a broadly effective layer range, though more fine-grained layer selection may further improve performance.<sup>1</sup>

<sup>1</sup>More analysis experiments, future directions, and limitations are provided in the supplementary materials.

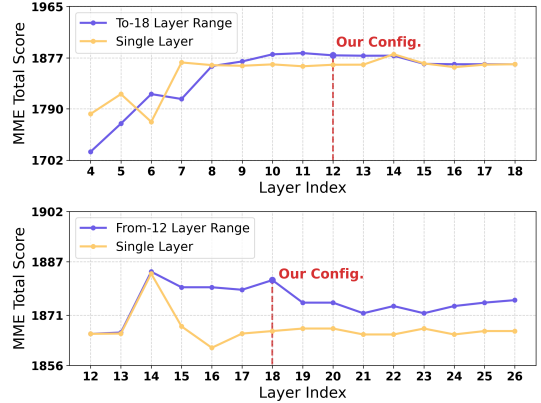


Figure 7. Performance changes on the total MME score with different layer ranges. The top panel varies the starting layer up to layer 18, while the bottom panel varies the ending layer from layer 12. Purple lines indicate performance across layer ranges, and yellow lines show performance when dynamic operations are applied to a single layer.

## 5. Related Work

**Multimodal Large Language Models.** Driven by the success of large language models (LLMs), increasing attention has been devoted to developing end-to-end multimodal large language models (MLLMs). Early works such as CLIP [38] and ALIGN [21] aligned visual and textual representations through contrastive learning, laying the foundation for cross-modal understanding. Following this paradigm, MLLMs typically employ a vision encoder and a projector to map visual embeddings into the language space of an LLM. Representative models such as BLIP-2 [28], LLaVA [31], InternVL [10] and the Qwen-VL [3] series adopt this modular design, where projected visual tokens and textual embeddings are jointly processed by the LLM for multimodal tasks. While this unified token-based framework enables generalization across modalities, it overlooks the inherent differences between visual and textual information. As a result, MLLMs often exhibit insufficient visual perception and hallucinated reasoning [5, 15, 22, 42], and their performance on multimodal reasoning tasks remains highly dependent on accurate visual grounding [11, 45]. This motivates further investigation into enhancing the visual perception and grounding capabilities of MLLMs to ensure reliable multimodal understanding.

**Visual Perception Enhancement of MLLMs.** To address these limitations, recent works have explored enhancing the visual perception of MLLMs through region selection, feature refinement, or adaptive attention, dynamically adjusting visual focus without retraining the backbone. V\* [45] introduces a guided visual search mechanism that leverages LLM knowledge for efficient querying and collaborative reasoning. DyFo [27] employs a dynamic focusing

module to refine spatial attention on task-relevant regions. Other methods improve fine-grained perception by cropping, recomposing, or re-encoding image regions. For example, ViCrop [51] identifies informative patches via attention maps from fixed layers, while Visual Perception Token [49] enhances focus through region-level cropping and re-encoding, and other works [16, 19] perform parameter-level expansion. Although effective, these approaches generally rely on fixed-layer attention or post-hoc modules and often require multiple forward passes, preventing adaptive refinement of regions of interest within a single inference and limiting both flexibility and efficiency.

## 6. Conclusion

In this work, we propose Blink, a dynamic visual token resolution framework that emulates human-like scanning and focusing within a single forward pass of MLLMs. Inspired by our two key insights on the visual attention shifts across layers and the benefits of allocating more computation to salient regions, Blink leverages saliency-guided scanning and dynamic token resolution to selectively expand important visual tokens and drop less relevant ones, enabling adaptive visual perception. Comprehensive experiments on downstream tasks and further analyses validate the effectiveness of the framework and its consistent improvements, elucidating the underlying mechanisms and showing the soundness of our method.

## References

- [1] Josh Achiam, Steven Adler, Sandhini Agarwal, Lama Ahmad, Ilge Akkaya, Florencia Leoni Aleman, Diogo Almeida, Janko Altenschmidt, Sam Altman, Shyamal Anadkat, et al. Gpt-4 technical report. *arXiv preprint arXiv:2303.08774*, 2023. 1
- [2] Jean-Baptiste Alayrac, Jeff Donahue, Pauline Luc, Antoine Miech, Iain Barr, Yana Hasson, Karel Lenc, Arthur Mensch, Katherine Millican, Malcolm Reynolds, et al. Flamingo: a visual language model for few-shot learning. *Advances in neural information processing systems*, 35:23716–23736, 2022. 1
- [3] Jinze Bai, Shuai Bai, Shusheng Yang, Shijie Wang, Sinan Tan, Peng Wang, Junyang Lin, Chang Zhou, and Jingren Zhou. Qwen-vl: A versatile vision-language model for understanding, localization, text reading, and beyond, 2023. 8
- [4] Shuai Bai, Keqin Chen, Xuejing Liu, Jialin Wang, Wenbin Ge, Sibo Song, Kai Dang, Peng Wang, Shijie Wang, Jun Tang, et al. Qwen2. 5-vl technical report. *arXiv preprint arXiv:2502.13923*, 2025. 1
- [5] Zechen Bai, Pichao Wang, Tianjun Xiao, Tong He, Zongbo Han, Zheng Zhang, and Mike Zheng Shou. Hallucination of multimodal large language models: A survey, 2025. 1, 8
- [6] Guizhen Chen, Weiwen Xu, Hao Zhang, Hou Pong Chan, Deli Zhao, Anh Tuan Luu, and Yu Rong. Geopqa: Bridging the visual perception gap in mllms for geometric reasoning, 2025. 2
- [7] Liang Chen, Haozhe Zhao, Tianyu Liu, Shuai Bai, Junyang Lin, Chang Zhou, and Baobao Chang. An image is worth 1/2 tokens after layer 2: Plug-and-play inference acceleration for large vision-language models. In *European Conference on Computer Vision*, pages 19–35. Springer, 2024. 3
- [8] Yilong Chen, Guoxia Wang, Junyuan Shang, Shiyao Cui, Zhenyu Zhang, Tingwen Liu, Shuohuan Wang, Yu Sun, Dianhai Yu, and Hua Wu. Nacl: A general and effective kv cache eviction framework for llms at inference time, 2024. 3
- [9] Yilong Chen, Junyuan Shang, Zhenyu Zhang, Yanxi Xie, Jiawei Sheng, Tingwen Liu, Shuohuan Wang, Yu Sun, Hua Wu, and Haifeng Wang. Inner thinking transformer: Leveraging dynamic depth scaling to foster adaptive internal thinking, 2025. 2
- [10] Zhe Chen, Jiannan Wu, Wenhui Wang, Weijie Su, Guo Chen, Sen Xing, Muyan Zhong, Qinglong Zhang, Xizhou Zhu, Lewei Lu, et al. Internvl: Scaling up vision foundation models and aligning for generic visual-linguistic tasks. In *Proceedings of the IEEE/CVF conference on computer vision and pattern recognition*, pages 24185–24198, 2024. 1, 8
- [11] An-Chieh Cheng, Hongxu Yin, Yang Fu, Qiushan Guo, Ruihan Yang, Jan Kautz, Xiaolong Wang, and Sifei Liu. Spatial-rgrpt: Grounded spatial reasoning in vision language models, 2024. 1, 8
- [12] Gregory Davis. Atlas: Mapping attention’s location and size to probe five modes of serial and parallel search. *Attention, Perception, & Psychophysics*, 86(6):1938–1962, 2024. 2
- [13] Chao Dong, Chen Change Loy, Kaiming He, and Xiaoou Tang. Image super-resolution using deep convolutional networks. *IEEE transactions on pattern analysis and machine intelligence*, 38(2):295–307, 2015. 5
- [14] Chao Dong, Chen Change Loy, and Xiaoou Tang. Accelerating the super-resolution convolutional neural network. In *European conference on computer vision*, pages 391–407. Springer, 2016. 5
- [15] Alessandro Favero, Luca Zancato, Matthew Trager, Siddharth Choudhary, Pramuditha Perera, Alessandro Achille, Ashwin Swaminathan, and Stefano Soatto. Multi-modal hallucination control by visual information grounding, 2024. 1, 8
- [16] Yuchen Feng, Bowen Shen, Naibin Gu, Jiaxuan Zhao, Peng Fu, Zheng Lin, and Weiping Wang. Dive into moe: Diversity-enhanced reconstruction of large language models from dense into mixture-of-experts. *arXiv preprint arXiv:2506.09351*, 2025. 9
- [17] Chaoyou Fu, Peixian Chen, Yunhang Shen, Yulei Qin, Mengdan Zhang, Xu Lin, Jinrui Yang, Xiawu Zheng, Ke Li, Xing Sun, Yunsheng Wu, Rongrong Ji, Caifeng Shan, and Ran He. Mme: A comprehensive evaluation benchmark for multimodal large language models, 2025. 3, 6
- [18] Leon Gmeindl, Yu-Chin Chiu, Michael S Esterman, Adam S Greenberg, Susan M Courtney, and Steven Yantis. Tracking the will to attend: Cortical activity indexes self-generated, voluntary shifts of attention. *Attention, Perception, & Psychophysics*, 78(7):2176–2184, 2016. 2
- [19] Naibin Gu, Zhenyu Zhang, Xiyu Liu, Peng Fu, Zheng Lin, Shuohuan Wang, Yu Sun, Hua Wu, Weiping Wang, and

Haifeng Wang. Beamlora: Beam-constraint low-rank adaptation. In *Proceedings of the 63rd Annual Meeting of the Association for Computational Linguistics (Volume 1: Long Papers)*, pages 11871–11883, 2025. 9

[20] Drew A Hudson and Christopher D Manning. Gqa: A new dataset for real-world visual reasoning and compositional question answering. In *Proceedings of the IEEE/CVF conference on computer vision and pattern recognition*, pages 6700–6709, 2019. 6

[21] Chao Jia, Yinfai Yang, Ye Xia, Yi-Ting Chen, Zarana Parekh, Hieu Pham, Quoc Le, Yun-Hsuan Sung, Zhen Li, and Tom Duerig. Scaling up visual and vision-language representation learning with noisy text supervision. In *International conference on machine learning*, pages 4904–4916. PMLR, 2021. 8

[22] Chaoya Jiang, Haiyang Xu, Mengfan Dong, Jiaxing Chen, Wei Ye, Ming Yan, Qinghao Ye, Ji Zhang, Fei Huang, and Shikun Zhang. Hallucination augmented contrastive learning for multimodal large language model, 2024. 1, 8

[23] Todd A Kelley, John T Serences, Barry Giesbrecht, and Steven Yantis. Cortical mechanisms for shifting and holding visuospatial attention. *Cerebral cortex*, 18(1):114–125, 2008. 2

[24] Jiwon Kim, Jung Kwon Lee, and Kyoung Mu Lee. Accurate image super-resolution using very deep convolutional networks. In *Proceedings of the IEEE conference on computer vision and pattern recognition*, pages 1646–1654, 2016. 5

[25] Ranjay Krishna, Yuke Zhu, Oliver Groth, Justin Johnson, Kenji Hata, Joshua Kravitz, Stephanie Chen, Yannis Kalantidis, Li-Jia Li, David A Shamma, et al. Visual genome: Connecting language and vision using crowdsourced dense image annotations. *International journal of computer vision*, 123(1):32–73, 2017. 6

[26] Bo Li, Yuanhan Zhang, Dong Guo, Renrui Zhang, Feng Li, Hao Zhang, Kaichen Zhang, Peiyuan Zhang, Yanwei Li, Ziwei Liu, et al. Llava-onevision: Easy visual task transfer. *arXiv preprint arXiv:2408.03326*, 2024. 1

[27] Geng Li, Jinglin Xu, Yunzhen Zhao, and Yuxin Peng. Dyfo: A training-free dynamic focus visual search for enhancing lmms in fine-grained visual understanding. In *Proceedings of the Computer Vision and Pattern Recognition Conference*, pages 9098–9108, 2025. 2, 8

[28] Junnan Li, Dongxu Li, Silvio Savarese, and Steven Hoi. Blip-2: Bootstrapping language-image pre-training with frozen image encoders and large language models. In *International conference on machine learning*, pages 19730–19742. PMLR, 2023. 1, 8

[29] Yifan Li, Yifan Du, Kun Zhou, Jinpeng Wang, Wayne Xin Zhao, and Ji-Rong Wen. Evaluating object hallucination in large vision-language models. *arXiv preprint arXiv:2305.10355*, 2023. 6

[30] Tsung-Yi Lin, Michael Maire, Serge Belongie, James Hays, Pietro Perona, Deva Ramanan, Piotr Dollár, and C Lawrence Zitnick. Microsoft coco: Common objects in context. In *European conference on computer vision*, pages 740–755. Springer, 2014. 6

[31] Haotian Liu, Chunyuan Li, Qingyang Wu, and Yong Jae Lee. Visual instruction tuning. *Advances in neural information processing systems*, 36:34892–34916, 2023. 8

[32] Haotian Liu, Chunyuan Li, Yuheng Li, and Yong Jae Lee. Improved baselines with visual instruction tuning. In *Proceedings of the IEEE/CVF conference on computer vision and pattern recognition*, pages 26296–26306, 2024. 1, 2, 6

[33] Haotian Liu, Chunyuan Li, Yuheng Li, Bo Li, Yuanhan Zhang, Sheng Shen, and Yong Jae Lee. Llava-next: Improved reasoning, ocr, and world knowledge, 2024. 1

[34] Yuan Liu, Haodong Duan, Yuanhan Zhang, Bo Li, Songyang Zhang, Wangbo Zhao, Yike Yuan, Jiaqi Wang, Conghui He, Ziwei Liu, et al. Mmbench: Is your multi-modal model an all-around player? In *European conference on computer vision*, pages 216–233. Springer, 2024. 6

[35] Pan Lu, Swaroop Mishra, Tanglin Xia, Liang Qiu, Kai-Wei Chang, Song-Chun Zhu, Oyvind Tafjord, Peter Clark, and Ashwin Kalyan. Learn to explain: Multimodal reasoning via thought chains for science question answering. *Advances in Neural Information Processing Systems*, 35:2507–2521, 2022. 6

[36] John HR Maunsell. Neuronal mechanisms of visual attention. *Annual review of vision science*, 1(1):373–391, 2015. 2

[37] Anand Mishra, Shashank Shekhar, Ajeet Kumar Singh, and Anirban Chakraborty. Ocr-vqa: Visual question answering by reading text in images. In *2019 international conference on document analysis and recognition (ICDAR)*, pages 947–952. IEEE, 2019. 6

[38] Alec Radford, Jong Wook Kim, Chris Hallacy, Aditya Ramesh, Gabriel Goh, Sandhini Agarwal, Girish Sastry, Amanda Askell, Pamela Mishkin, Jack Clark, et al. Learning transferable visual models from natural language supervision. In *International conference on machine learning*, pages 8748–8763. PMLR, 2021. 8

[39] Jeff Rasley, Samyam Rajbhandari, Olatunji Ruwase, and Yuxiong He. Deepspeed: System optimizations enable training deep learning models with over 100 billion parameters. In *KDD '20: The 26th ACM SIGKDD Conference on Knowledge Discovery and Data Mining, Virtual Event, CA, USA, August 23-27, 2020*, pages 3505–3506. ACM, 2020. 1

[40] Amanpreet Singh, Vivek Natarajan, Meet Shah, Yu Jiang, Xinlei Chen, Dhruv Batra, Devi Parikh, and Marcus Rohrbach. Towards vqa models that can read. In *Proceedings of the IEEE/CVF conference on computer vision and pattern recognition*, pages 8317–8326, 2019. 6

[41] Gemini Team, Petko Georgiev, Ving Ian Lei, Ryan Burnell, Libin Bai, Anmol Gulati, Garrett Tanzer, Damien Vincent, Zhufeng Pan, Shibo Wang, et al. Gemini 1.5: Unlocking multimodal understanding across millions of tokens of context. *arXiv preprint arXiv:2403.05530*, 2024. 1

[42] Shengbang Tong, Zhuang Liu, Yuexiang Zhai, Yi Ma, Yann LeCun, and Saining Xie. Eyes wide shut? exploring the visual shortcomings of multimodal llms, 2024. 1, 8

[43] Dezhao Tu, Danylo Vashchilenko, Yuzhe Lu, and Panpan Xu. Vl-cache: Sparsity and modality-aware kv cache compression for vision-language model inference acceleration. *arXiv preprint arXiv:2410.23317*, 2024. 3

[44] Thomas Wolf, Lysandre Debut, Victor Sanh, Julien Chau-  
mond, Clement Delangue, Anthony Moi, Pierric Cistac, Tim  
Rault, Remi Louf, Morgan Funtowicz, Joe Davison, Sam  
Shleifer, Patrick von Platen, Clara Ma, Yacine Jernite, Julien  
Plu, Canwen Xu, Teven Le Scao, Sylvain Gugger, Mariama  
Drame, Quentin Lhoest, and Alexander Rush. Transformers:  
State-of-the-art natural language processing. In *Proceedings  
of the 2020 Conference on Empirical Methods in Natural  
Language Processing: System Demonstrations*, pages 38–  
45, Online, 2020. Association for Computational Linguis-  
tics. 1

[45] Penghao Wu and Saining Xie. V\*: Guided visual search  
as a core mechanism in multimodal llms, 2023. URL  
<https://arxiv.org/abs/2312.14135>, 5. 1, 2, 8

[46] Qiong Wu, Xiangcong Yang, Yiyi Zhou, Chenxin Fang,  
Baiyang Song, Xiaoshuai Sun, and Rongrong Ji. Grounded  
chain-of-thought for multimodal large language models,  
2025. 2

[47] Long Xing, Qidong Huang, Xiaoyi Dong, Jiajie Lu, Pan  
Zhang, Yuhang Zang, Yuhang Cao, Conghui He, Jiaqi Wang,  
Feng Wu, et al. Pyramiddrop: Accelerating your large  
vision-language models via pyramid visual redundancy re-  
duction. *arXiv preprint arXiv:2410.17247*, 2024. 3

[48] Weihao Ye, Qiong Wu, Wenhao Lin, and Yiyi Zhou. Fit and  
prune: Fast and training-free visual token pruning for multi-  
modal large language models. In *Proceedings of the AAAI  
Conference on Artificial Intelligence*, pages 22128–22136,  
2025. 3

[49] Runpeng Yu, Xinyin Ma, and Xinchao Wang. Introducing vi-  
sual perception token into multimodal large language model.  
*arXiv preprint arXiv:2502.17425*, 2025. 2, 9

[50] Weihao Yu, Zhengyuan Yang, Linjie Li, Jianfeng Wang,  
Kevin Lin, Zicheng Liu, Xinchao Wang, and Lijuan Wang.  
Mm-vet: Evaluating large multimodal models for integrated  
capabilities. *arXiv preprint arXiv:2308.02490*, 2023. 6

[51] Jiarui Zhang, Mahyar Khayatkhoei, Prateek Chhikara, and  
Filip Ilievski. Mllms know where to look: Training-free per-  
ception of small visual details with multimodal llms. *arXiv  
preprint arXiv:2502.17422*, 2025. 2, 9

[52] Shan Zhang, Aotian Chen, Yanpeng Sun, Jindong Gu, Yi-  
Yu Zheng, Piotr Koniusz, Kai Zou, Anton van den Hengel,  
and Yuan Xue. Open eyes, then reason: Fine-grained visual  
mathematical understanding in mllms, 2025. 2

# Blink: Dynamic Visual Token Resolution for Enhanced Multimodal Understanding

## Supplementary Material

### A. Training Details

#### A.1. Configurations

For each involved transformer layer, we attach a lightweight token super-resolution (TokenSR) module to refine the expanded saliency tokens. Each TokenSR module consists of three sequential convolutional layers. The input and output channels are both set to 4096, matching the hidden dimension of the MLLM backbone, while the intermediate layers use 2048 and 1024 channels, respectively. The convolution kernel sizes are 5, 3, and 1, each applied with symmetric padding to preserve spatial resolution.

#### A.2. Datasets

To train the TokenSR modules, we use the processed LLaVA-1.5 [32] training set, which is constructed from several widely used vision–language datasets. For each image, we additionally generate four quadrant crops (top-left, top-right, bottom-left, bottom-right) and record their positions relative to the original image. Each processed sample therefore consists of the full image, one cropped quadrant, and its corresponding positional metadata.

During training, both the full image and the cropped quadrant are converted into pixel-value tensors and fed through the frozen MLLM backbone to obtain their hidden representations. The cropped image provides the teacher features, while the TokenSR module operates on the full-image tokens to generate expanded tokens. The module is optimized so that these expanded tokens match the teacher features at the corresponding spatial region.

#### A.3. Hyper-parameters

Training Parameter	Value
# GPUs	2
Sequence length	1024
Data type	Bfloat16
Learning rate	1e-4
Learning rate scheduler	Cosine
Warmup ratio	0.03
Optimizer	AdamW
Global batch size	8
Epoch	1
DeepSpeed	Zero-2

Table 4. Training parameters used in the experiments.

The training hyper-parameters for the TokenSR modules are presented in Table 4. All experiments are conducted on 8 H800 (80G) GPUs in total, where each TokenSR module is trained on 2 GPUs with a global batch size of 8, using BFloat16 precision. We set the warmup ratio to 3% and employ a cosine learning rate scheduler, decaying the learning rate from 1e-4 to 0. Our implementation is based on HuggingFace Transformers [44] and DeepSpeed [39].

### B. Implementation Details

In our main experiments in Sec. 4, the inference settings are configured as follows. For the layer ranges and saliency thresholds, we use layers 12–18 with  $\tau_{\text{exp}} = 0.5$  and  $\tau_{\text{drop}} = 0.4$  for MME and MM-Vet. For GQA, the same layer range is used with  $\tau_{\text{exp}} = 0.6$  and  $\tau_{\text{drop}} = 0.4$ . For POPE, we apply layer 18 with  $\tau_{\text{exp}} = 0.5$  and  $\tau_{\text{drop}} = 0.4$ . For MMBench, MMBench-CN and ScienceQA, we use the same layer with  $\tau_{\text{exp}} = 0.25$ .

Additionally, in the ablation studies on the MME benchmark, the High  $\tau_{\text{exp}}$  / Low  $\tau_{\text{drop}}$  setting corresponds to values of 0.7 and 0.3, respectively. The High  $\tau_{\text{exp}}$  configuration refers to using  $\tau_{\text{exp}} = 0.7$  while keeping  $\tau_{\text{drop}}$  fixed at 0.4, consistent with the main experiment on MME.

### C. Evaluation on Other Backbone

We further evaluate Blink on the LLaVA-NeXT-7B [33] backbone. For POPE, MMBench, MMBench-CN, GQA, ScienceQA, and MM-Vet, we use layers 14–20 with  $\tau_{\text{exp}} = 0.5$  and  $\tau_{\text{drop}} = 0.4$ , while for MME, we use layers 12–20 with thresholds  $\tau_{\text{exp}} = 0.4$  and  $\tau_{\text{drop}} = 0.3$ . As shown in Table 5, our method consistently improves performance across a wide range of downstream benchmarks. Blink yields a notable gain of 15.00 on MMECognition compared with the vanilla model and achieves the highest scores on GQA, MMBench-CN, POPE, and MM-Vet. Although its MMEPerception score is slightly lower than that of Blink-interp, Blink shows stronger advantages on most tasks, suggesting that the fully trained TokenSR module strengthens fine-grained multimodal understanding.

Blink-interp achieves the best performance on MMEPerception and improves over the backbone model on ScienceQA and MM-Vet, highlighting the complementary benefits of the dynamic inference pipeline. These results collectively demonstrate that Blink generalizes well to stronger backbones and provides robust gains across diverse downstream tasks.

Method	MME <sub>Perception</sub>										
	Exist.	Count	Pos.	Color	Poster	Celeb.	Scene	Landm.	Artw.	OCR	Total
Vanilla	195.00	<b>158.33</b>	<b>135.00</b>	175.00	150.68	146.47	<b>164.25</b>	<b>167.50</b>	<b>134.75</b>	<b>102.50</b>	1529.48
<i>Blink</i> -interp (Ours)	195.00	<b>158.33</b>	<b>135.00</b>	<b>180.00</b>	150.68	<b>147.35</b>	<b>164.25</b>	<b>167.50</b>	134.00	<b>102.50</b>	<b>1534.62</b>
<i>Blink</i> (Ours)	<b>200.00</b>	<b>158.33</b>	130.00	<b>180.00</b>	<b>153.74</b>	142.94	163.50	166.00	134.00	<b>102.50</b>	1531.02

Method	MME <sub>Cognition</sub>					GQA	MMBench	MMBench <sub>CN</sub>	POPE	SQA <sub>Img</sub>	MM-Vet
	CS	Num	Text	Code	Total						
Vanilla	<b>120.00</b>	<b>57.50</b>	102.50	<b>35.00</b>	315.00	64.26	<b>69.07</b>	60.82	86.37	70.40	39.80
<i>Blink</i> -interp (Ours)	<b>120.00</b>	55.00	110.00	<b>35.00</b>	320.00	64.22	<b>69.07</b>	60.82	86.23	<b>70.50</b>	40.40
<i>Blink</i> (Ours)	<b>120.00</b>	<b>57.50</b>	<b>117.50</b>	<b>35.00</b>	<b>330.00</b>	<b>64.29</b>	<b>69.07</b>	<b>60.91</b>	<b>86.40</b>	70.45	<b>40.50</b>

Table 5. Downstream task performance across multiple benchmarks on LLaVA-NeXT. Vanilla denotes the base model, and our methods correspond to two configurations of Blink, where -interp indicates the variant that replaces the amplifier with training-free interpolation while retaining the Blink inference pipeline. The best scores are in **bold**.

## D. Cases of Attention Redistribution

Following the analysis in Sec. 4.4, we conduct additional visualization experiments to examine how the tokens generated by the TokenSR module influence attention redistribution across transformer layers after expansion. As in the main experiments, expansion is applied at layer 12, and the newly generated tokens are preserved in all subsequent layers without being dropped.

Fig. 8 presents attention maps across different layers to illustrate this spatial redistribution. We analyze the two examples from Sec. 2.2, along with four additional cases. As expected, in all examples, attention on the newly introduced tokens remains more evenly distributed compared to the original visual tokens. Furthermore, in the first three cases, we observe clear layer-wise shifts in attention, consistent with our first key insight that the model progressively adjusts its attention allocation across layers after the expanded tokens are introduced.

## E. Ablation Study on Patch Numbers

In our main experimental setup, the reshaped  $H \times W$  attention grid used in saliency-guided scanning is uniformly partitioned into  $2 \times 2$  patches. In this section, we evaluate the effect of varying the partition granularity by dividing the grid into  $p \times p$  non-overlapping patches of equal size, and report results on the MME benchmark.

Since changing the number of patches alters the minimum proportion of the image that a salient region can occupy, we scale the saliency ratio thresholds accordingly. For the expansion threshold, the patch-adjusted value is computed as  $\tau_{\text{exp}}^{(p)} = 0.5 \times \frac{1/p^2}{1/2^2}$ , and similarly for the drop threshold,  $\tau_{\text{drop}}^{(p)} = 0.4 \times \frac{1/p^2}{1/2^2}$ .

Method	# Patches	Perc.	Cogn.	Total
<i>Blink</i> -interp	$2 \times 2$	1514.08	353.21	1867.29
	$3 \times 3$	1507.44	350.36	1857.80
	$4 \times 4$	1499.38	335.36	1834.74
<i>Blink</i>	$2 \times 2$	1519.74	361.79	1881.53
	$3 \times 3$	1498.16	374.64	1872.80
	$4 \times 4$	1500.24	358.21	1858.45

Table 6. Performance of Blink and its interpolation variant on the MME benchmark with different numbers of patches. The  $2 \times 2$  setting is used in our main configuration, and the other configurations correspond to alternative patch partition settings.

As shown in Table 6, neither the  $3 \times 3$  nor  $4 \times 4$  partitioning yields improvements over the default  $2 \times 2$  setting. For Blink-interp, increasing the number of patches consistently degrades both perception and cognition scores, with the  $4 \times 4$  configuration showing the largest decline. For Blink, the  $3 \times 3$  variant offers a small gain in cognition but still reduces perception and overall MME performance, while the  $4 \times 4$  setup leads to drops across all metrics. This may be because the current thresholds are derived using a simple proportional scaling rule, and more fine-grained tuning could further optimize performance for different patch granularities. Nevertheless, across all configurations, Blink equipped with the trained TokenSR module consistently outperforms Blink-interp, confirming that the learned amplifier is more effective than naive interpolation under all patch partitions.

Layers	Perc.	Cogn.	Total
<i>Blink-interp (Ours)</i>	1514.08	353.21	1867.29
w/o interp	1510.58 <sub>-3.50</sub>	357.86 <sub>+4.65</sub>	1868.44 <sub>+1.15</sub>
<i>Blink (Ours)</i>	1519.74	361.79	1881.53
w/o interp	1515.08 <sub>-4.66</sub>	355.00 <sub>-6.79</sub>	1870.08 <sub>-11.45</sub>

Table 7. Performance of Blink and its training-free variant on the MME benchmark with and without the interpolation step. In the w/o interp setting, the selected saliency tokens are inserted directly without being upsampled to match the original image resolution.

## F. Ablation Study on Interpolation

In our method, prior to feeding saliency tokens into the TokenSR module, we first perform interpolation to upsample these tokens. The purpose of this interpolation is to align the length of the salient token sequence with that of the original image tokens, allowing both training and inference to proceed directly with standard two-image inputs at the original spatial resolution. This design ensures that the model operates on inputs that preserve the original spatial structure, which is more consistent with conventional visual encoding practices and facilitates effective learning of fine-grained multimodal representations.

Table 7 presents the performance on the MME benchmark with and without the interpolation step. In our experiments, the w/o interp condition refers to bypassing this initial upsampling. Specifically, after selecting the saliency tokens, they are directly extracted and inserted between the original visual and text tokens without resizing. For Blink-interp, w/o interp corresponds to inserting the saliency tokens directly into the dynamic inference pipeline without any training. For Blink, w/o interp means feeding the tokens into the trained TokenSR module without prior interpolation. From the experimental results, skipping interpolation for Blink-interp slightly reduces the perception score by 3.50, indicating that aligning the length of the expanded saliency sequence with the original image helps preserve spatial information. For Blink, removing interpolation leads to drops of 4.66 in perception, 6.79 in cognition, and 11.45 overall, further demonstrating that the TokenSR module benefits from receiving saliency tokens of the same length as the original image tokens, which allows the amplifier to more effectively refine multimodal representations. Overall, these results highlight that interpolation is a crucial step for fully leveraging spatial context and ensuring stable and accurate performance.

## G. Limitations and Future Work

Although Blink demonstrates strong generalization across different tasks and backbones, its current design relies pri-

marily on convolution-based upsampling. Exploring alternative expansion modules may further improve flexibility and performance. Moreover, due to computational constraints, all experiments are conducted on models no larger than 7B parameters, leaving the scalability of Blink to larger MLLMs unverified.

Future work will explore alternative TokenSR mechanisms, such as multi-layer perceptrons, as complements or replacements for the convolution-based module, and investigate improvements that enhance the overall efficiency and practicality of Blink.

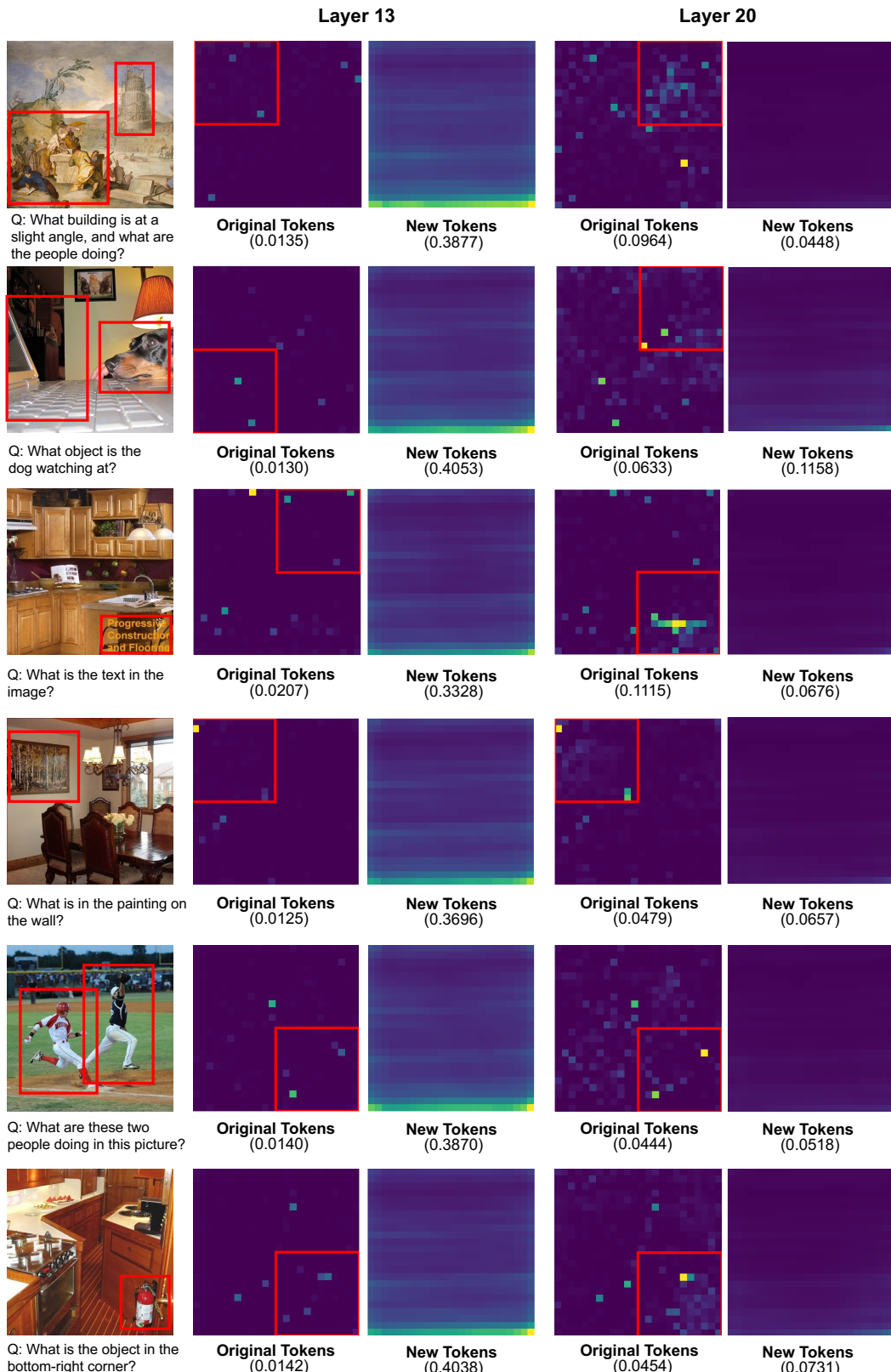


Figure 8. Visualization of attention redistribution after token expansion. Red boxes in the original image indicate the ground-truth important regions. The right panels show attention distributions on the original and expanded visual tokens at layers 13 and 20.